A&A manuscript no.
(will be inserted by hand later)

Your thesaurus codes are:
08(02.01.2; 09.01.1; 09.09.1 RCW103; 09.19.2; 11.19.2; 13.09.4)

ASTRONOMY AND ASTROPHYSICS

Infrared spectroscopy of young supernova remnants heavily interacting with the interstellar medium *

I. Ionized species in RCW103

E. Oliva[1], **A.F.M Moorwood**[2], **S. Drapatz**[3], **D. Lutz**[3], **and E. Sturm**[3]

[1] Osservatorio Astrofisico di Arcetri, Largo E. Fermi 5, I–50125 Firenze, Italy
[2] European Southern Observatory, Karl Schwarzschild Str. 2, D-85748 Garching bei München, Federal Republic of Germany
[3] Max Planck Institute für Extraterrestrische Physik, Postfach 1603, D-85740 Garching, Germany

Received 16 October, accepted ... December 1998

Abstract. ISO spectral observations of the supernova remnant RCW103 are presented. This object is the prototype of relatively young remnants ($\sim 10^3$ yr) with fast shocks ($v_s \sim 1000$ km/s) interacting with dense interstellar medium.

The spectrum is dominated by prominent lines of [NeII], [SiII], [FeII] and other low excitation species which provide, for the first time, a simple and reliable estimate of the gas abundances of refractory (Si, Fe, Ni) and non–refractory (Ne, P, S, Cl, Ar) species. Apart from nickel, all the derived abundances are close to solar, confirming that the shock has destroyed all dust grains. Like the optical nickel lines, [NiII]λ6.64 μm yields Ni abundances a factor $\simeq$10 solar which we propose results from a large underestimation of the computed Ni^+ collision strengths.

The observed intensities and velocity widths of ionic lines are compatible with emission from the post–shock region alone with only a very small (if any) contribution from the photoionized precursor. This result does not agree with shock models which predict that the precursor should emit powerful line emission, especially from highly ionized species. The possible consequence of this on the modelling of Seyfert spectra is briefly discussed.

Key words: Atomic data; ISM: abundances; ISM: supernova remnants; Galaxies: Seyfert; Infrared: ISM: lines and bands

1. Introduction

Radiative supernova remnants are the ideal astrophysical laboratory for studying the emission spectrum of relatively fast shocks interacting with the interstellar medium (e.g. Draine & McKee 1993). In the standard, idealized, view the supernova blast wave expands through a uniform, low density ($\approx$1 cm^{-3}) medium and the shock remains adiabatic, i.e. the postshock gas has insufficient time to cool/recombine, for $>10^4$ yr and up until the shock has slowed to $v_s < 200$ km/s. After this the shock becomes radiative with the postshock region recombining and radiating away most of the shock mechanical energy in the form of UV, optical and IR lines whose surface brightness simply scale with the shock energy flux $n\,v_s^3$, n being the pre–shock density. In practice, a 'standard' radiative supernova remnant is expected to emit weak lines, i.e. $\Sigma(\mathrm{H}\beta)\lesssim 10^{-5}$ erg cm^{-2} s^{-1} sr^{-1} (cf. Sect 3.2 of Dopita & Sutherland 1996, hereafter DS96) and 2–3 orders of magnitude weaker than those observed in bright supernovae remnants such as RCW103 (Oliva et al. 1989, hereafter OMD89). This simple fact indicates, therefore, that the shock of RCW103 is much faster or, equivalently, that the SNR is much younger than the canonical values. This is also confirmed by X–ray spectra which yield an age of only 10^3 yr and a main shock velocity of about 1200 km/s (Nugent et al. 1984).

Thus, the prominent line emission from the optical filaments of RCW103 results from the impact of the $v_s \sim 1000$ km/s SNR blast wave onto dense clouds of ISM material (probably molecular clouds). Due to the higher density, the postshock gas cools and recombines much faster than in the canonical model and the SNR becomes radiative at much earlier times. The large surface brightness of the emitted line spectrum simply reflects the large mechanical energy flux of the shock.

Studying the IR spectrum of radiative shocks can give interesting information on the metal abundances and, by comparing refractory and non–refractory species, can yield a direct measurement of the actual efficiency of grain destruction by the shock. Moreover, the spectra can be used to verify the predictions of models of fast shocks, which have been recently published by DS96.

Send offprint requests to: E. Oliva

* Based on observations with ISO, an ESA project with instruments funded by ESA Member States (especially the PI countries: France, Germany, the Netherlands and the United Kingdom) and with the participation of ISAS and NASA.

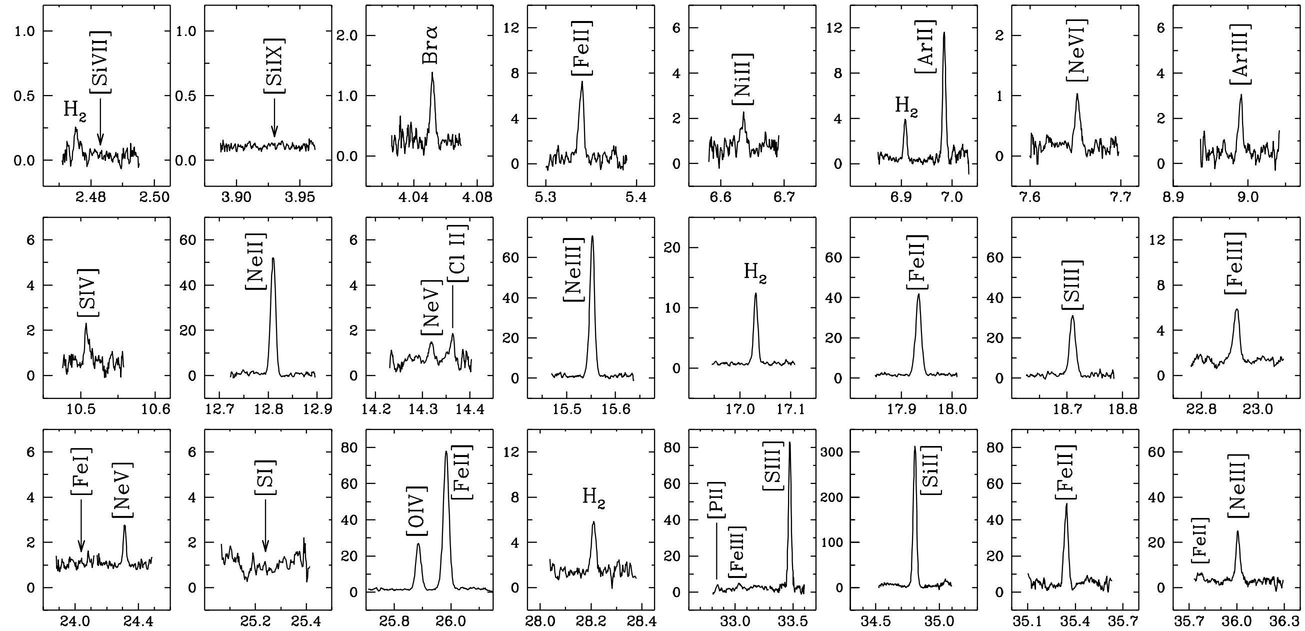

Fig. 1. Individual line scans with SWS02. Wavelengths are in μm and fluxes in Jy. Arrows mark the positions of undetected lines.

Being the brightest and best studied SNR, RCW103 was chosen as the prototype object for ISO template spectra of gas excited by fast shocks. The observations are described in Sect. 2 and the derived physical parameters are discussed in Sect. 3. The results are compared with shock model predictions in Sect. 4 where we draw particular attention to the relative roles of the photoionized precursor and post–shock region in producing the observed lines.

2. Observations and results

2.1. ISO spectroscopy

Complete SWS01 (speed 4, 6700 sec total integration time) and LWS01 (4400 sec total integration time, no background spectrum subtracted) spectra centered at the peak of [FeII]1.644 μm line emission (cf. Fig. 7) were obtained on February 6 and February 20, 1996. These were complemented by a quick PHT-S spectrum (448 sec, February 20) and deeper SWS02 observations at selected wavelengths (total 7000 sec, obtained on August 15, 1996 and February 17, 1997), always centered at the same position. The short wavelength section (2.5–5 μm) of the PHT-S spectrum was strongly contaminated by detector memory effects (a very bright source was observed just before RCW103), the PHT-SS results are therefore unreliable and not presented here.

The SWS data were reduced using standard routines of the SWS interactive analysis system (IA) using calibration tables as of September 1997. Reduction relied mainly on the default pipeline steps, plus removal of signal spikes, elimination of the most noisy band 3 detectors, and flat–fielding. The LWS spectrum is based on the end–product of the automatic pipeline as of April 1997 (i.e. OLP 6). A post-processing was performed within the ISO Spectral Analysis Package (ISAP)[1], Version 1.2, with special emphasis on removal of signal spikes and memory effects, averaging of the different scans, and flat-fielding of the 10 detectors.

The final rebinned spectra are displayed in Figs. 1 to 4 and the derived line fluxes are listed in Table 1 together with additional information. Note that most of the lines in the 2.4–40 μm range were observed twice, i.e. in the complete SWS01 spectrum (Fig. 2) and in the deeper SWS02 line scans (Fig. 1). The derived fluxes were always within $\pm$30% and in most cases equal to much better than 20%. The errors quoted in Table 1 also include the differences between the two measurements. It should be noted that, to the best of our knowledge, the transitions of [ClII]λ14.36 and [PII]λ32.8 are newly detected astronomical lines. Of interest is also the marginal detection of an unidentified feature at 74.2 μm whose position and flux are remarkably similar to those found in the spectrum of NGC7027 (Liu et al. 1996).

The SWS spectrum (Figs. 1, 2) is characterized by prominent lines over a faint continuum (about 0.5 Jy at 10 μm) while emission by cold dust is evident in the LWS spectrum (Fig. 3). The level of the 100 μm continuum is similar to the background IRAS level reported by Arendt (1989) and the continuum seen in the LWS spectrum is, therefore, probably dominated by back/foreground emission from the galaxy disk. The same applies to the PAH's features visible in the PHT-S spectrum (Fig. 4) and to the

[1] The ISO Spectral Analysis Package (ISAP) is a joint development by the LWS and SWS Instrument Teams and Data Centers. Contributing institutes are CESR, IAS, IPAC, MPE, RAL and SRON.

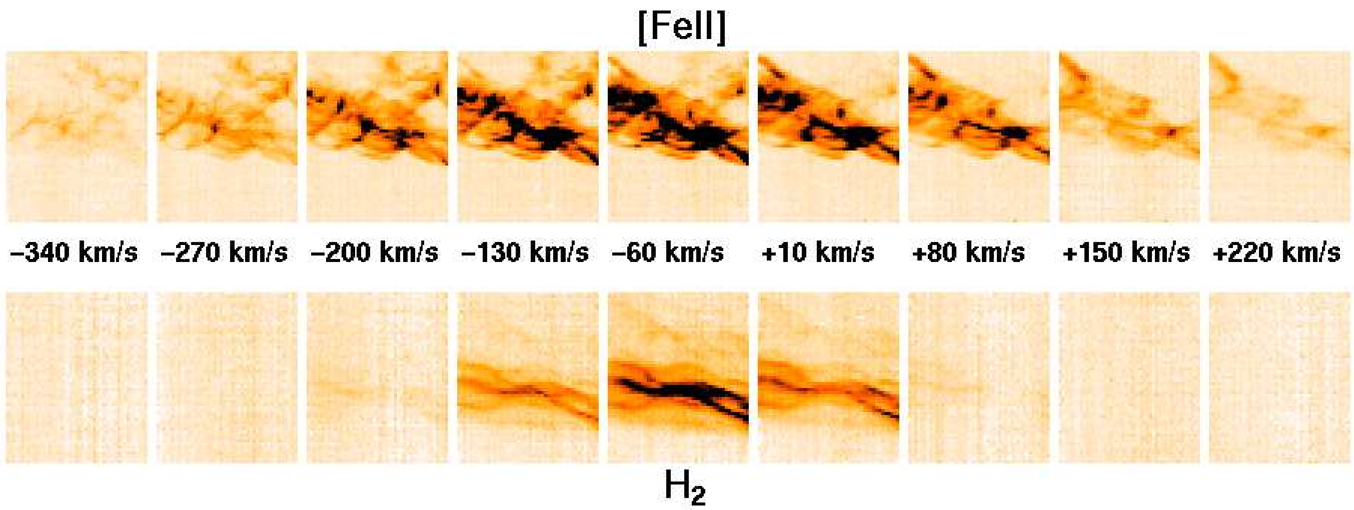

Fig. 5. Line images at various velocity bins, reconstructed from the IRSPEC spectra discussed in Sect. 2, all frames are cut to the same levels as the v=–60 km/s images. Note that [FeII] (1.644 μm) shows bright filaments moving by up to $\pm$250 km/s, while H_2 (2.121 μm) is narrow and unresolved (i.e. FWHM<130 km/s). The colour images are also available at http://www.arcetri.astro.it/~oliva

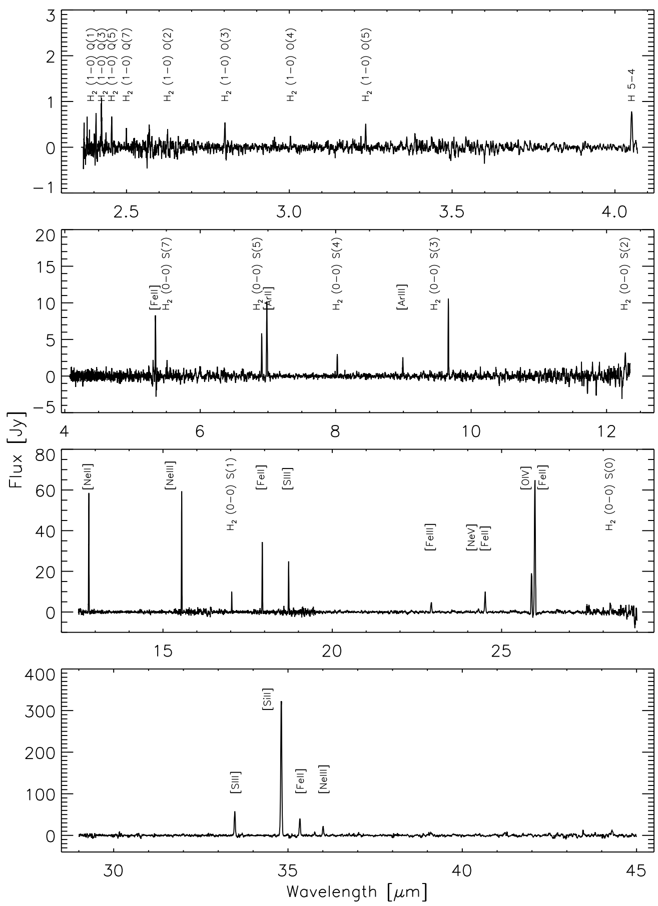

Fig. 2. Complete 2.4-45 μm SWS01 spectrum with line identification. Note that each spectral segment has been "continuum subtracted" to remove instrumental offsets and drifts. The continuum level can be estimated from the PHT-S spectrum (Fig. 4) and from the deeper SWS02 line scans (Fig. 1).

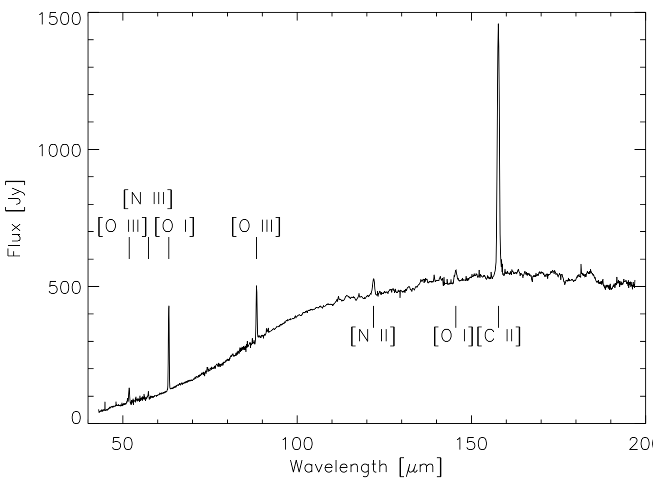

Fig. 3. Complete LWS01 spectrum with lines identification. Note that RCW103 lies close to the the Galactic plane (b = −0.36). Therefore, the 100 μm continuum and the [OI], [CII], [NII] lines are strongly contaminated, and most probably dominated by fore/background emission.

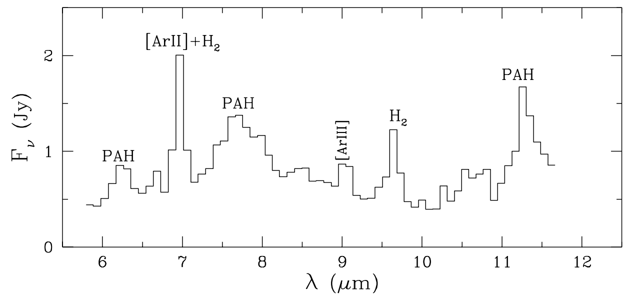

Fig. 4. Complete PHT-SL spectrum. The PAH features are most probably dominated by fore/background emission from the Galaxy disk.

Table 1. Observed ISO line fluxes

Line	Flux[(1)]	A_λ[(2)]	Slit[(3)]	Aper. corr.[(4)]
[SiVII]λ2.483	<1.2	0.38	14 × 20	1.0
[SiIX]λ3.936	<0.5	0.17	14 × 20	1.0
Brα λ4.051	7 (1)	0.16	14 × 20	1.0
[FeII]λ5.340	57 (17)	0.10	14 × 20	1.0
[NiII]λ6.635	6 (1.5)	0.07	14 × 20	1.0
[ArII]λ6.985	62 (12)	0.06	14 × 20	1.0
[NiIII]λ7.349	<3	0.06	14 × 20	1.0
Pfα λ7.458	<3	0.06	14 × 20	1.0
[NeVI]λ7.655	1.6 (.3)	0.06	14 × 20	1.0
[ArIII]λ8.990	7 (1)	0.04	14 × 20	1.0
[SIV]λ10.51	2 (.5)	∼0.5[b]	14 × 20	1.0
[NeII]λ12.81	120 (10)	–	14 × 27	.85
[NeV]λ14.32	1.3 (.3)	–	14 × 27	.85
[ClII]λ14.36	1.7 (.4)	–	14 × 27	.85
[NeIII]λ15.56	107 (10)	–	14 × 27	.85
[FeII]λ17.93	51 (6)	–	14 × 27	.85
[SIII]λ18.71	35 (4)	–	14 × 27	.85
[FeIII]λ22.92	8 (1)	–	14 × 27	.85
[FeI]λ24.04	<1	–	14 × 27	.85
[NeV]λ24.32	1.9 (.3)	–	14 × 27	.85
[FeII]λ24.51	13 (3)[a]	–	14 × 27	.85
[SI]λ25.24	<1	–	14 × 27	.85
[OIV]λ25.88	27 (3)	–	14 × 27	.85
[FeII]λ25.98	90 (10)	–	14 × 27	.85
[PII]λ32.8	2 (.6)	–	20 × 33	.58
[FeIII]λ33.0	2 (.6)	–	20 × 33	.58
[SIII]λ33.47	57 (6)	–	20 × 33	.58
[SiII]λ34.8	280 (40)	–	20 × 33	.58
[FeII]λ35.34	36 (4)	–	20 × 33	.58
[FeII]λ35.77	3 (.8)	–	20 × 33	.58
[NeIII]λ36.01	15 (3)	–	20 × 33	.58
[OIII]λ51.7	190 (30)	–	⊘ 80	–
[NIII]λ57.3	57 (14)	–	⊘ 80	–
[OI]λ63.2[c]	710 (80)[c]	–	⊘ 80	–
Unidentified λ74.2[d]	22 (7)	–	⊘ 80	–
[OIII]λ88.2	220 (30)	–	⊘ 80	–
[NII]λ121[c]	75 (13)[c]	–	⊘ 80	–
[OI]λ145[c]	33 (7)[c]	–	⊘ 80	–
[CII]λ157[c]	630 (70)[c]	–	⊘ 80	–

(1) Observed line flux, units of 10^{-20} W cm^{-2}, errors are given in parenthesis

(2) Extinction (mag) extrapolated from A_H=0.75 (OMD90) using $A_\lambda \approx \lambda^{-1.7}$ up to 9 μm. Reddening is assumed to be negligible beyond 12 μm

(3) Size (in arcsec) of the SWS (λ<45 μm) and LWS (λ>45 μm) apertures

(4) Correction factor to account for different apertures, based on the IRSPEC map of [FeII]λ1.644 (see caption of Fig. 7).

a Only SWS01 measurement available

b Adopting a "standard" A(silicate feature)/$A_V \simeq$0.1 ratio

c Line flux is probably contaminated by back/foreground galactic emission

d Unidentified feature also seen in NGC7027 (Liu et al. 1996)

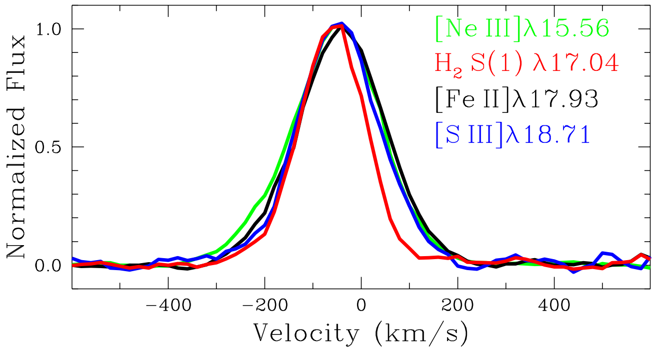

Fig. 6. Normalized profiles of FIR lines falling at wavelengths where the SWS spectrometer achieves its highest spectral resolution. The nominal resolving power for extended sources is 222, 198, 186 and 175 km/s for the [NeIII], H_2, [FeII] and [SIII] lines, respectively. The ionic lines are all resolved and significantly broader than H_2 which is narrow and unresolved. This result agrees with the ground based velocity maps (Fig. 5) and indicate that the ionized lines are produced downstream of the shock front, while H_2 arises from the precursor (see text, Sect. 2).

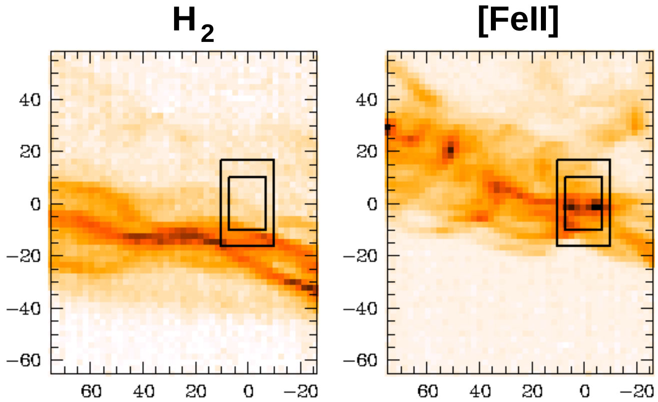

Fig. 7. Line images of H_2 (2.121 μm) and [FeII] (1.644 μm) reconstructed from the IRSPEC spectra described in Sect. 2. Coordinates are arcsec from the 'ionized peak' where all the ISO spectra presented here were centered. The sizes of the black rectangles correspond to the smallest and largest slits of SWS. The ground based [FeII]λ1.644 flux is 70, 82, and 120 ($\times 10^{-20}$ W cm^{-2}) in the 14x20, 14x27 and 20x33 sqarcsec SWS apertures, respectively. These numbers are used to compute the aperture correction factors listed in Table 1.

[OI]λ63.2, [NII]λ121 and [CII]λ157 lines which are likely to be strongly contaminated by emission from the diffuse ISM.

Given the relatively large extinction towards RCW103, i.e. $A_H \simeq 0.75$ or $A_V \simeq 4.5$ (cf. Oliva et al. 1990, hereafter OMD90), the reddening corrections are not negligible for the lines at the shortest wavelengths. Therefore, in Table 1 we also list the extinctions values which were derived assuming a 'typical' reddening curve, i.e. $\tau \approx \lambda^{-1.75}$ outside of the silicate band. The largest and most uncertain correction is for [SIV]λ10.52 which lies within the silicate band and for which we have assumed A(10μm)/A$_V$$\simeq$0.1.

Useful dynamical information can be derived from the profiles of the lines between 15 and 19 μm, the wavelength range where SWS02 grating spectra achieve their highest spectral resolution. The instrumental resolution depends on the size of the source along the dispersion direction and varies, for example, between 120 and 175 km/s for a compact and extended [SIII]λ18.7 source, respectively. Luckily, the SWS slit was almost exactly aligned N–S and was, therefore, roughly uniformly illuminated in the dispersion (E–W) direction (cf. Fig. 7). The observed line profiles are displayed in Fig. 6. The ionic lines are resolved and exhibit similar profiles, within the errors, but are broader than the H_2 line which is unresolved. This agrees well with the higher spatial resolution velocity maps from the NIR data discussed below.

2.2. *Ground based near infrared spectroscopy*

Near infrared observations were collected in Jan 1992 at the ESO–NTT using the long–slit spectrometer IRSPEC equipped with a 62x58 SBRC InSb array whose pixel size was 2.2$''$ along the slit and $\simeq$5 Å along the dispersion direction. Line images of [FeII]λ1.644 and H_2 λ2.121 were reconstructed from 57 spectra with the 100$''$ x 2.2$''$ slit aligned E-W and shifted by steps of 2.2$''$ along the N-S direction. Each long-slit spectrum consisted of a single on–chip integration of 30 sec with sky exposures every 10 spectra.

The integrated line images are displayed in Fig. 7 whose caption also include results of [FeII] aperture photometry which has been used to determine the correction factors for the different beams used by SWS (see also Table 1). These assume that all ionized species have spatial distribution similar to [FeII] which is justified by the following arguments.

– The flux of Brα seen by ISO is within <10% of the value extrapolated from the ground based measurement (OMD90) assuming a constant [FeII]/Brα ratio over the region of interest.

– The morphology of the [FeII] filaments is virtually identical to those seen in optical line images (cf. e.g. Moorwood et al. 1987).

It should be noted, however, that the H_2 lines arise from a totally different region $\sim$20$''$ south of the ionized gas and outside the optical/radio/X–ray remnant, as originally found by OMD89. This indicates that H_2 emission traces material which has not yet been reached by the shock, most probably a molecular cloud heated by the soft X–rays from the shock front (cf. OMD90).

Fig. 5 shows images at various velocity bins, each roughly corresponding to the wavelength range covered by 1 pixel. Evident are the high velocity [FeII] filaments whose projected velocities extend up to $\pm$250 km/s and

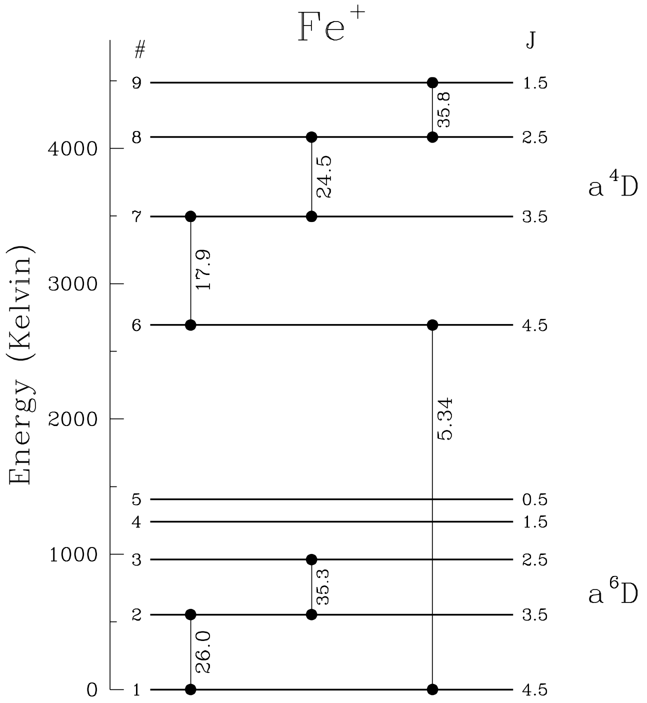

Fig. 8. Energy level diagram showing the paths of the [FeII] lines detected by ISO. The near IR lines come from higher energy levels which are visualized in Fig. 6b of OMD90.

are compatible with the idea that this line is produced downstream of the fast shock (cf. the Introduction). The H_2 filaments, on the contrary, do not show evidence of motions larger than the FWHM=130 km/s instrumental resolution.

3. Physical parameters of the emitting gas

3.1. *Temperature and density*

The ISO spectra include several density and/or temperature sensitive line pairs. Besides the well known, n_e–sensitive [OIII], [NeIII], [NeV] and [SIII] fine structure lines, useful transitions are those of [FeII] whose paths are displayed in Fig. 8, while their dependence on T_e and n_e is visualized in Fig. 9. Note that the ratios [FeII]λ35.3/λ26.0 and [FeII]λ24.5/λ17.9 are also density sensitive, but vary by only a factor $\simeq$1.7 between the low and the high density limits so the resulting n_e is highly uncertain.

The deduced values of T_e and n_e are summarized in Table 2 where the most remarkable result is the large spread of densities deduced from the various diagnostic ratios. The lowest value is from the [OIII] lines which are measured through the much larger LWS beam (cf. Table 1) and are probably affected by the emission of a diffuse, lower density component. Some of the discrepancies between the [FeII] densities could also reflect density and temperature stratification. In particular, the ground state line at 26.0 μm could partially arise from excitation by collisions with atomic hydrogen in regions far down-

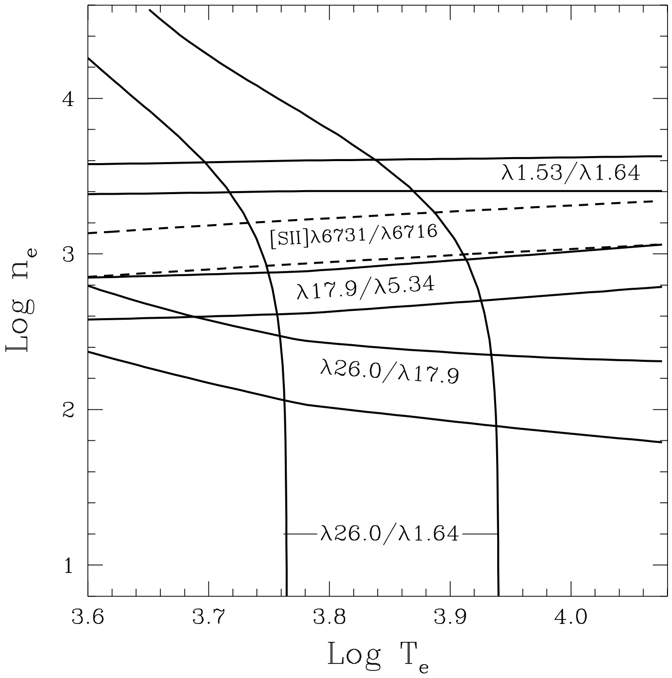

Fig. 9. Contour plots of the [SII] and [FeII] diagnostic line ratios listed in Table 2. The curves for [FeII] are computed using the collision strengths of Pradhan & Zhang (1993) and the transition probabilities of Nussbaumer & Storey (1988) and Quinet et al. (1996).

Table 2. Diagnostic line ratios

Line ratio	Observed[(1)]	n_e[(2)] (cm^{-3})	T_e[(2)] ($x10^3$ K)
[OIII]λ51.7/λ88.2	$-.07 \pm .09$	30–250	–
[NeIII]λ15.6/λ36.0	$1.0 \pm .08$	$\leq$5000	–
[NeIII]λ3869/λ15.6[a]	$-.40 \pm .20$	–	8.3–10.5
[NeV]λ14.3/λ24.3	$-.15 \pm .13$	$\leq$5000	–
[SIII]λ18.7/λ33.5	$-.05 \pm .08$	$\leq$1200	–
[SIII]λ9531λ18.7[a]	$-.31 \pm .20$	–	7.1–13.8
[SII]λ6731/λ6716[b]	$.11 \pm .05$	800–2000	–
[FeII]λ35.3/λ26.0	$-.56 \pm .09$	any	–
[FeII]λ24.5/λ17.9	$-.60 \pm .11$	any	–
[FeII]λ17.9/λ5.34	$-.16 \pm .13$	400–1000	–
[FeII]λ17.9/λ26.0	$-.24 \pm .07$	80–320	
[FeII]λ26.0/λ1.64[c]	$-.26 \pm .13$	–	5.2–8.7
[FeII]λ1.53/λ1.64[d]	$-.92 \pm .06$	2500–4100	–

(1) Log of observed ratio, including aperture and reddening corrections (cf. Table 1 and Sect. 2)

(2) Deduced gas density and temperature, see also Fig. 9

[a] From [NeIII]λ3869/Hβ=0.41 (Leibowitz & Danziger 1983) and [SIII]λ9531/Hβ=0.16 (Dennefeld 1986) adopting the case–B Hβ/Brα=13 ratio

[b] [SII] lines from Leibowitz & Danziger (1983)

[c] Flux of [FeII]1.644 from IRSPEC image (cf. caption of Fig. 7) corrected for extinction using A_H=0.75

[d] Near infrared [FeII] lines from OMD90

stream of the shock where the temperature is too low to produce the other [FeII] lines. However, such a cold component should primarily show up in the temperature sensitive [FeII]λ26.0/λ1.64 ratio which, on the contrary, yields a relatively high value for T_e and therefore implies that any cold component can account, at most, for 30% of the observed flux of [FeII]λ26.0. An alternative explanation is that the different [FeII] densities simply reflect relatively small uncertainties in the atomic parameters of Fe^+ which, for example, overestimate the critical density of [FeII]λ1.53 and of the other satellite lines in the near infrared.

It should be noted that much larger discrepancies between the [FeII] densities from FIR and NIR line ratios were found from observations of the Galactic center (GC, Lutz et al. 1996) where, however, all the [FeII] lines but one are reasonably well explained by a collisionally excited plasma with $T_e\sim$8000 K and n_e=10^{3-4} cm^{-3}. The only line which does not fit is λ17.9 which is a factor of $\simeq$10 lower than predicted. This cannot be easily explained neither by alternative excitation mechanisms such as e.g. UV pumping (Lucy private communication) nor by advocating large uncertainties on the collision strengths which are ruled out by the results presented here. A partial explanation to the "GC anomaly" could be to assume that the foreground extinction at 17.9 μm is a factor of 2–3 larger than that predicted from the standard reddening curve.

The [NeIII], [NeV] and [SIII] ground state lines ratios are compatible, within the errors, with their low density limits, but useful estimates of temperature can be obtained including measurements of optical transitions from the same ions. The values listed in Table 2 are derived from the available fluxes of optical and FIR lines relative to Hβ and Brα, respectively, and assume a generous error of $\pm$0.2 dex to include e.g. possible uncertainties in the reddening correction of the optical data. The resulting temperatures are quite well constrained, nevertheless, and the values are compatible with those predicted for the post–shock region of shocks with velocities $\geq$300 km/s (cf. Tables 3A–3D of DS96). Note in particular that slower shocks are predicted to have a post–shock [NeIII] temperature of 15–30 $\times 10^3$ K and significantly hotter than the observed value.

The temperature of [NeV] is of particular interest to verify if this ion is produced downstream of the shock, in which case NeV is predicted to be collisionally ionized in plasma at about $3.5\,10^5$ K, or in the much cooler ($< 2\,10^4$ K) photoionized precursor. In the first case one expects [NeV]λ3426/λ14.3=8 or, equivalently, [NeV]λ3426/Hβ=0.1, while values a factor of 6–7 lower are expected if the emission is from the precursor. Unfortunately, no observation of [NeV]λ3426 is available in the literature and, given the quite high extinction, measurements at the required depth (a few % of Hβ) are not straightforward.

Table 3. Relative abundances

Lines used(1)	Abundance ratio(2)	Solar value
[FeIII]22.9/[FeII]26.0	$[Fe^{++}/Fe^{+}] = -0.99$	–
[NeIII]15.6/[NeII]12.8	$[Ne^{++}/Ne^{+}] = -0.47$	–
[ArIII]8.99/[ArII]6.98	$[Ar^{++}/Ar^{+}] = -0.72$	–
[SIV]10.5/[SIII]18.7	$[S^{+3}/S^{++}] = -1.5$:	–
[NIII]57.3/[OIII]51.7	$[N^{++}/O^{++}] = -0.6$:	$[N/O] = -0.89$
[NeII]12.8/Brα	$[Ne^{+}/H^{+}] = -3.7$:	$[Ne/H] = -3.93$
[SiII]34.8/[NeII]12.8	$[Si^{+}/Ne^{+}] = -0.66$	$[Si/Ne] = -0.51$
[PII]32.8/[NeII]12.8	$[P^{+}/Ne^{+}] = -2.6$:	$[P/Ne] = -2.6$
[SIII]18.7/[NeIII]15.6	$[S^{++}/Ne^{++}] = -1.0$	$[S/Ne] = -0.86$
[ClII]14.4/[NeII]12.8	$[Cl^{+}/Ne^{+}] = -2.59$	$[Cl/Ne] = -2.5$
[ArII]6.98/[NeII]12.8	$[Ar^{+}/Ne^{+}] = -1.39$	$[Ar/Ne] = -1.47$
[FeII]17.9/[NeII]12.8	$[Fe^{+}/Ne^{+}] = -0.62$	$[Fe/Ne] = -0.55$
[NiII]6.64/[NeII]12.8	$[Ni^{+}/Ne^{+}] = -1.03$	$[Ni/Ne] = -1.82$

(1) Fluxes from Table 1 including aperture and reddening corrections

(2) Logaritmic values, typical uncertainties are ±0.12 dex except for those marked with a column which are ±0.25 dex

3.2. Abundances

A specific advantage of FIR lines is that their emissivities depend very little on the gas temperature and abundances derived from these lines are, therefore, little affected by uncertainties in the assumed value of T_e. Also, to minimize the effect of density variations, we selected for each ion the line with the largest critical density which, for most species, was $\gg 10^3$ cm^{-3} and larger than the values of n_e derived above. The derived abundances are listed in Table 3 where the quoted errors also include generous uncertainties on temperature (i.e. T_e=5000–10000 K and T_e=7000–15000 K for singly and double ionized species, respectively) and density ($n_e = 0-4000$ cm^{-3}).

The most remarkable result is that, apart for the anomaly of nickel which is discussed below, all the metal abundances are close to the solar values. This indicates that the emitting gas is indeed ISM material in which the dust grains have been destroyed by the shock front thus returning all the refractory species (Si, Fe) into the gas phase. It should also be noted that, to the best of our knowledge, the ISO data provide for the first time a measurement of the abundances of phosphorus and chlorine in any supernova remnant. Moreover, the abundance of silicon from the FIR [SiII] line is much less uncertain than those normally derived from UV lines whose intensities strongly depend on the assumed gas temperature (e.g. Russel & Dopita 1990).

3.2.1. The nickel anomaly

The relatively large strength of the optical [NiII]λ7379 line in SNRs and other nebulae has long puzzled astronomers because it requires a Ni^{+}/Fe^{+} abundance ratio a factor ~10 larger than the cosmic value. A similar overabundance, i.e. $[Ni^{+}/Fe^{+}]=-0.41$ dex or a factor of 7 above the solar $[Ni/Fe]=-1.27$ value, is inferred here from the [NiII]λ6.64 ground state transition (cf. Table 3). This result is very difficult to understand because the line emitting gas is shock excited interstellar material which should not have, therefore, an anomalous Ni abundance. A number of explanations for the optical result have been proposed (cf. Bautista et al. 1996 for a recent review). These include:

– Selective dust depletion of Fe relative to Ni, which cannot hold in our case because most of the iron is in the gas phase.

– Low Fe^{+}/Fe relative abundances, which can be excluded because most of the iron is in the form of Fe^{+} (cf. Table 3).

– Contribution by UV fluorescence to the [NiII] lines, which could be important for the optical lines but has negligible effect on the [NiII]λ6.64 ground state transition (cf. Table 1 of Lucy 1995). Also, no obvious source of strong UV radiation exists in RCW103 (cf. Sect. 4.1.3 of OMD90).

– Density stratification with low n_e regions emitting [SII], higher density gas emitting [FeII] and the densest (~10^6 cm^{-3}) regions dominating [NiII] whose lines have the highest critical density (Bautista et al. 1996). However, such a high density component should also (but does not) show up in other lines with high critical density, in particular [NeII]λ12.8 which has $n_{crit} = 6\,10^5$ cm^{-3} and only a factor of 10 lower than the critical density of the [NiII]λ6.64 line. Since the [NiII]/[NeII] ratio also requires a nickel overabundance of a factor of 6 (cf. Table 3), and considering also the relatively low densities derived from the [FeII] lines (cf. Table 2), one is forced to assume that most of the nickel is in regions with densities $\gtrsim 10^7$ cm^{-3} while all the other species, including Fe, must be in regions with densities $< 10^4$ cm^{-3}, which is implausible.

We therefore conclude that the apparently large Ni^{+}/Fe^{+} relative abundance simply reflects uncertainties in the collision strengths for [NiII] whose computed values are systematically a factor ≈10 lower than those of [FeII]. In particular, the collision strength of the [NiII]λ6.64 ground state line is only Υ=0.15 and by far (i.e. a factor of >5) lower than the collision strengths of the main ground state transitions of any other astrophysical abundant species. Adopting, for example, Υ=1.0 for the [NiII]λ6.64 transition would yield $[Ni^{+}/Ne^{+}]=-1.85$ and $[Ni^{+}/Fe^{+}]=-1.18$, i.e. values within 0.1 dex of the solar Ni/Ne and Ni/Fe relative abundances.

4. Discussion

4.1. Comparison with shock models

Explicit predictions for a few FIR lines have been included in the models for relatively slow ($\lesssim$150 km/s) shock interacting with low density material by Raymond (1979) and Shull & McKee (1979). The first lists [NeII], [SiII] and

[FeII] while the latter include [SiII], [SIII] and [SIV]. The predicted line ratios from the above mentioned models are not in good agreement with our results. In particular, the observed [SIV]/[SIII] ratio is a factor >5 larger than the computed values. Also, most models predict a factor of >3 too strong [SiII] (relative to [NeII], [FeII], [SIII]), but this could be attributed to uncertainties in the atomic parameters of SiII which have been updated several times since the publication of the shock model results. The most important discrepancy, however, is that the predicted surface brightnesses are always a factor >10 lower than the observed values, which simply reflects the fact that the shock of RCW103 is much faster than the values used in the above models (cf. the Introduction and below).

Models of slow shocks interacting with very dense gas ($n \geq 10^3$ cm^{-3}) were developed by Hollenbach & McKee (1989) who also include explicit predictions for all the FIR lines of singly ionized and neutral species. The main problem with these models is that they span preshock densities much larger than the <300 cm^{-3} required to account for the measured electron densities in the post–shock region. Consequently, lines with low critical densities, e.g. [SiII], are predicted too faint. Moreover, the models underestimate the flux of [FeII] lines by a factor of ∼5.

The most recent models of DS96, which cover shock velocities of 200–500 km/s and are more representative of the conditions of RCW103, do not however give explicit predictions for the FIR lines. Nevertheless, reasonably accurate line ratios can be computed from the values of ionic column densities and mean temperatures listed in the above paper. To a first approximation, the ratio of two lines from the post–shock region is

$$\frac{I_1}{I_2} = \frac{N_1\, j_1(T_1)}{N_2\, j_2(T_2)} \tag{1}$$

where N and T are the column densities and temperature of the emitting ions and j is the line emission coefficient which, for FIR lines, is very little dependent on the gas temperature. The contribution from the photoionized precursor can be also computed from the published tables of N and T in the pre–shock region, while the compression factor (i.e. the ratio between the electron density in the post and pre shock regions) can be estimated imposing that the regions have similar Hβ surface brightnesses (cf. Sect. 3.2 of DS96), i.e.

$$[n_e\, N_p]_{precursor} = [n_e\, N_p]_{post-shock} \tag{2}$$

Out of the many FIR line ratios we have identified those which are most sensitive to the shock speed and to the presence of the photoionized precursor. The behaviour of the selected line ratios is plotted in Fig. 10 where the most remarkable result is that models including the emission from the precursor largely overpredict the strength of [SIV] and [NeV]. The velocity dependence of the [NeV]/[NeIII] ratio in the post–shock region may appear at first sight surprising, but can be easily understood as follows. The post–shock [NeV] emission always occurs in collisionally ionized gas at $T \simeq 3.5\,10^5$ K and whose column density, which primarily depends on the shape of the gas cooling curve, does not strongly vary with the shock speed. The [NeIII] line, on the contrary, could be strongly enhanced by emission from photoionized gas in the post–shock region, but this only occurs at $v \gtrsim 300$ km/s while slower shocks do not produce enough ionizing photons to support a large NeIII zone. In short, the sharp decrease of [NeV]/[NeIII] between 200 and 300 km/s is because the [NeIII] line emission rapidly increases in this velocity interval.

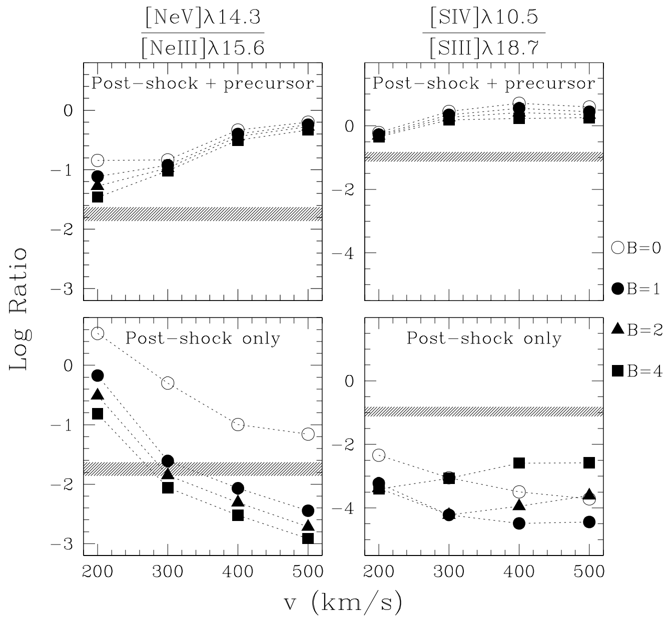

Fig. 10. Behaviour of velocity and precursor sensitive line ratios. The theoretical values are computed from the shock models of DS96 as described in Sect. 4.1. B=$B/\sqrt{n}$ is the magnetic parameter (cf. DS96) and the dashed regions show the observed values.

The main conclusion of this analysis is that all ionic lines can be reasonably well reproduced by post–shock emission. This conclusion also agrees with the broad line profiles observed by SWS (Sect. 2.1) and imaging–spectroscopy observations of [OIII]λ5007 which show complex dynamical structures, similar to those seen in [FeII] (Fig. 5) and incompatible with emission from the precursor (Moorwood et al. 1987). The only ionic line which cannot be accounted for by post–shock emission is [SIV] which should be a factor of >10 fainter, but can be reproduced adding a quite 'incomplete precursor', i.e. ≃5% the SIV column density of the precursor predicted by the DS96 models (cf. Fig. 10).

Given the importance that the photoionized precursor may have in modelling the spectra of active galaxy nuclei (Sect. 4.3), it is of interest to investigate why little or no ionic line emission is observed from the precursor of RCW103. We envisage the following possibilities.

– The precursor in RCW103 is very thin to UV ionizing photons, but this is very difficult to reconcile with the fact that H_2 emission is observed from pre–shock molecular gas lying outside of the shock front (cf. Fig. 7). For H_2 to exist, the molecules must be shielded from the strong field of UV ionizing radiation from the shock front or, equivalently, the preshock region must be optically thick.

– The shock front in RCW103 is significantly slower than so far assumed and below $\simeq$150 km/s, the minimum speed required to produce a prominent phototoionized precursor. This is in strict constrast with the observed line widths and filament dynamics (cf. Sect. 2 and Fig. 5). Moreover, slow shocks cannot explain the very large surface brightness of the lines which require a large mechanical power of the shock, i.e. a large $n\,v_s^3$ product, n being the preshock density and v_s the shock speed. More specifically, the average surface brightness of Brα within the ISO beam corresponds to $\Sigma(\mathrm{H}\beta)$=4 10^{-3} erg cm^{-2} s^{-1} sr^{-1} which, coupled to the predicted values from shock models (Eq. 3.4 of DS96), yields

$$\left(\frac{n}{100\ \mathrm{cm}^{-3}}\right)\left(\frac{v_s}{100\ \mathrm{km/s}}\right)^{2.4} \simeq 68\cos\theta \qquad (3)$$

or, equivalently, a shock speed of about $370\,(\cos\theta)^{0.42}$ km/s for a pre–shock density of 300 cm^{-3}. Larger pre–shock densities are effectively excluded by the measured electron densities (Table 2) in the post–shock region, i.e. after the gas has been compressed by the shock front. The factor $\cos\theta$ takes into account projection effects such as those modelled in details by Hester (1987) who interpreted the bright filaments in IC443 and Cygnus–Loop in therms of relatively slow shocks seen quasi edge–on and found that small filaments amplified by a factor 10–100 should be quite common. However, this model cannot hold for RCW103 for the following reasons. This remnant is much brighter (factor of >10) than IC443 and Cygnus–Loop. The *average* surface brightness within the relatively large ISO–SWS beam (i.e. the value used in Eq. 3) is already a factor of $\simeq$4 lower than that observed on arcsec scales in optical/IR line images of RCW103. The most largely amplified edge–on filaments should have small radial velocities (FWHM$\lesssim$40 km, cf. Fig. 2 of Hester 1987) amd this is not compatible with the observed line widths and dynamics.

– The shock models largely overpredict the contribution of the photoionized precursor. Indeed, DS96 state that the column density of ionized gas in the precursor might be overestimated due to a possibly incorrect treatment of the transfer of the UV ionizing photons (cf. end of Sect. 4.2 of DS96). Moreover, the ionization structure of the precursor could be much different than computed in DS96 if the shock evolves on time scales shorter than $\simeq$100 yr, i.e. the recombination time in the pre–shock gas.

Table 4. Comparison between RCW103 (SNR), the Galactic center and the Circinus galaxy

Line ratio	RCW103[(1)]	GC[(2)]	Circinus[(3)]
[FeIII]λ22.9/[FeII]λ26.0	0.089	3.7	–
[NeIII]λ15.6/[NeII]λ12.8	0.89	0.044	0.46
[NeV]λ14.3/[NeIII]λ15.6	0.012	–	1.0
[NeIII]λ15.6/[FeII]λ26.0	3.1	1.2	5.4
[OIV]λ25.9/[FeII]λ26.0	0.30	0.24	8.8
[SiIX]λ3.94/[SiII]λ34.8	<0.003	–	0.025

(1) Line fluxes from this paper
(2) Data from Lutz et al. (1996)
(3) Data from Moorwood et al. (1996)

4.2. Comparison with the Galactic center

The region on the line of sight of the GC has a rich spectrum of prominent IR lines which are believed to arise from gas with an unusually large Fe gas phase abundance and which is primarily photoionized by quite hot stars (Lutz et al. 1996). Table 4 is a comparison between the most significant line ratios measured in RCW103 and in the GC.

The [FeIII]λ22.9/[FeII]λ26.0 ratio is much higher (a factor of 42) in the GC spectrum. This implies $Fe^{++}/Fe^{+} > 1$ and a factor $\geq$10 larger than in RCW103, regardless of the assumed gas density in the GC. This simply reflects the fact that a region predominantly photoionized by stars, such as those near to the GC, contains only a relatively small fraction of partially ionized gas. The recombining region behind the SNR shock front, on the contrary, has a large zone of partially ionized gas, which is heated by photoionization from the shock front radiation, and where most of iron is forced into Fe^{+} by the very rapid charge exchange reactions with neutral hydrogen.

The [OIV]λ25.9/[FeII]λ26.0 ratio is the same in the two objects, within the errors. Given the difficulties to produce both FeII and OIV with photoionization from normal stars, it seems not unreasonable to conclude that both species are primarily produced by shock excited gas in the line of sight of the GC.

The [NeIII]λ15.6/[NeII]λ12.8 ratio is a factor of 20 lower in the GC than in RCW103 which indicates that fast shocks are more effective than late O stars in producing NeIII. Moreover, the [NeIII]λ15.6/[FeII]λ26.0 ratio is only a factor of 2.6 higher in the GC than in RCW103 and this indicates that a non negligible fraction of the [NeIII] emission from the GC could come from shock excited gas.

4.3. Photoionized precursor and shocks in active galaxy nuclei

According to the shock models of DS96, the precursor could be an important source of lines from high ionization species (e.g. [OIII]λ5007), but its importance relative to the post–shock region may strongly depend on the column density of the pre–shock material. In a paper specifically dedicated to study the spectral signatures of shocks in active galaxies, Dopita & Sutherland (1995) consider the following limiting cases:

– Shock only, in which the precursor is very thin and its emission is effectively negligible relative to the post–shock region. This can fairly well reproduce the line ratios observed in low excitation AGNs (LINERS).

– Shock + precursor, where the pre–shock region is opaque to the ionizing photons from the shock front. Since the ionizing spectrum is quite hard and effectively similar to a typical AGN spectrum, the ionization structure of the precursor is similar to that of standard narrow line regions photoionized by the AGN. Consequently, the emerging line spectrum is similar to that of standard photoionization models and could explain, therefore, the high excitation lines from e.g. type 2 Seyferts.

In view of this proposed scenario, it is interesting to compare the spectra of RCW103 with that of the Circinus galaxy, an archetype Seyfert 2 galaxy whose observed line ratios are listed in Table 4. The most striking difference is that the high excitation (coronal) lines are much stronger in Circinus with, in particular, [NeV]/[NeIII]=1 and roughly 2 orders of magnitude larger than in RCW103. Such a strong [NeV] could be in principle compatible with emission from the precursor of a $v\sim 500$ km/s shock (cf. Fig. 10), while even higher velocities, i.e. $\gtrsim$1000 km/s, could probably account for highest ionization coronal lines (e.g. [SiX]). The main problem is that these shocks should also emit prominent low excitation lines from their fast moving post–shock gas, but this is incompatible with the observed line profiles which are remarkably narrow (FWHM$\leq$150 km/s, Oliva et al. 1994) and similar for all ionization species. Therefore, a shock dominated model for the Circinus galaxy seems very unlikely and, more generally, the role played by the photoionized precursor in Seyferts could be questioned on the basis of the following arguments.

If dominated by photoionization, the low excitation lines from the post–shock region (e.g. [SII]) should be broader than those from the photoionized precursor (e.g. [OIII]), but this is in strict contrast with the observations which show that [OIII] and higher excitation lines are usually broader than those of [SII] and lower excitation species.

The ISM medium of Seyfert galaxies is well known to be quite "porous", especially within the ionization cones, and several arguments indicate that the line emitting clouds are probably density bounded (e.g. Binette et al. 1996). The host galaxies of LINERS, on the contrary, are often very rich in both gas and dust, a spectacular example being NGC4945 (e.g. Moorwood et al. 1996). It seems therefore curious that the shocks in Seyferts should primarily impact onto the relatively few large clouds (i.e. those with large enough column density to absorb all the ionizing photons from the shock) while, in LINERS, the shocks should selectively avoid the largest clouds and only hit regions with low column densities (i.e. those which cannot produce a bright precursor).

The absence of significant emission from the pre–shock region in RCW103 indicates that shock models may overestimate the importance of the precursor region.

5. Conclusions

We have presented IR spectroscopic observations of RCW103, a relatively young and fast (about 10^3 yr and $\simeq$1200 km/s, Nugent et al. 1984) supernova remnant whose prominent line emitting filaments result from the interaction of the fast SNR blast wave with ISM clouds. The secondary shocks driven into the higher density medium have velocities $\gtrsim$300 km/s, as indicated by the observed dynamics of the filaments (cf. Fig.5), by the very high surface brightness of the lines and by velocity sensitive line ratios such as [NeV]/[NeIII] (Sect. 4.1).

The spectrum is dominated by prominent lines from low excitation species which have been used to estimate the density, temperature and abundances of the emitting region. The results indicate this is post–shock gas with relatively low density ($n_e\sim 10^3$ cm^{-3}), normal ISM abundance and essentially free of dust. Although the [NiII] lines seem to require a large nickel overabundance we argue, however, that this simply reflects uncertainties in the atomic parameters and propose that the collision strength for [NiII]λ6.64 is Υ=1 and a factor of 7 larger than the computed value. Smaller uncertainties in some of the atomic parameters for [FeII] are also suggested by the data which nevertheless exclude large errors in the computed collision strengths.

An important discrepancy with fast shock models is that the prominent high excitation lines predicted from the photoionized precursor are not seen in RCW103. Since low column densities in the pre–shock region are ruled out by the observed H_2 emission from the shock precursor, this discrepancy probably indicates that shock models largely overestimate the strength of the lines from the precursor. This may cause problems to shock models of Seyfert galaxies where the high excitation lines should be dominated by emission from the photoionized pre–shock region.

Acknowledgements. E. Oliva acknowledges the partial support of the Italian Space Agency (ASI) through the grant ARS–98–116/22. We thank Henrik Spoon for help with the ISOPHOT-S data. SWS and the ISO Spectrometer Data Center at MPE are supported by DLR (formerly DARA) under grants 50–QI–8610–8 and 50–QI–9402–3.

References

Arendt R.G., 1989, ApJS 70, 1

Bautista M.A., Peng J., Pradhan A.K., 1996, ApJ 460, 372

Binette L., Wilson A. S., Storchi-Bergmann T., 1996, A&A 312, 365

Leibowitz E.M., Danziger I.J., 1983, MNRAS 204, 273

Dennefeld M., 1986, A&A 157, 267

Dopita M.A., Sutherland R.S., 1995, ApJ 455, 468

Dopita M.A., Sutherland R.S., 1996, ApJS 102, 161 (DS96)

Draine B.T., McKee C.F., 1993, ARA&A 31, 373

Hester J.J., 1987, ApJ 314, 187

Hollenbach D., McKee C.F., 1989, ApJ 342, 306

Liu X.W. et al., 1996, A&A 315, L257

Lucy L.B., 1995, A&A 294, 555

Lutz D. et al., 1996, A&A 315, L269

Moorwood A.F.M., Danziger I.J., Oliva E., 1987, The Messenger 48, 49

Moorwood A.F.M., van der Werf P.P., Kotilainen J.K., Marconi A., Oliva E., 1996 A&A **308**, L1

Moorwood A.F.M., Lutz D., Oliva E., Marconi A., Netzer H., Genzel R., Sturm E., de Graauw T., 1996, A&A 315, L109

Nugent J.J., Pravdo S.H., Garmire G.P., Becker R.H., Tuohy I.R., Winkler P.F, 1984, ApJ 284, 612

Nussbaumer H., Storey P.J., 1988, A&A 193, 333

Oliva E., Moorwood A.F.M., Danziger I.J., 1989, A&A 214, 307 (OMD89)

Oliva E., Moorwood A.F.M., Danziger I.J., 1989, A&A 240, 453 (OMD90)

Oliva E., Salvati M., Moorwood A.F.M., Marconi A., 1994, A&A 288, 457

Pradhan A.K., Zhang H.L., 1993, ApJL 409, L77

Quinet P., Le Dourneuf M., Zeippen C.J., 1996, A&AS 120, 361

Raymond J.C., 1979, ApJS 39, 1

Russel S.C., Dopita M.A., 1990, ApJS 74, 93

Shull J.M., McKee C.F., 1979, ApJ 227, 131